Journal of Rheology

RESEARCH ARTICLE | MAY 01 2022

Pair interactions between viscous drops in a viscoelastic matrix in free shear: Transition from passing to tumbling trajectories

Anik Tarafder; Abhilash Reddy Malipeddi ; Kausik Sarkar

J. Rheol. 66, 571–584 (2022)
https://doi.org/10.1122/8.0000374
CHORUS

Pair interactions between viscous drops in a viscoelastic matrix in free shear: Transition from passing to tumbling trajectories

Anik Tarafder, Abhilash Reddy Malipeddi, and Kausik Sarkar[a)]

Department of Mechanical and Aerospace Engineering, The George Washington University, Washington, DC 20052

(Received 24 September 2021; final revision received 20 February 2022; published 31 March 2022)

Abstract

Shear-induced pair interactions between viscous drops suspended in a viscoelastic matrix are numerically investigated examining the effects of elasticity and drop deformability on their post-collision trajectory. Two different trajectory types are identified depending on the Weissenberg number *Wi* and capillary number *Ca*. Drops suspended in a Newtonian matrix ($Wi = 0.0$) show a passing trajectory where drops slide past each other and separate in the stream-wise direction. However, when increasing the Weissenberg number above a critical value, a tumbling/doublet trajectory is observed where two drops rotate around the midpoint of the line joining their centers, as was also seen previously for rigid particles. The tumbling trajectory is explained by investigating the flow around a single drop in shear. Elasticity generates a larger region of spiraling streamlines around a drop, which, during a pair interaction, traps the second drop giving rise to the tumbling pair. Decreasing deformability (lower *Ca*) and increasing viscoelasticity (higher *Wi*) favor a tumbling trajectory. With simulations sweeping the parameter space, we obtain a phase plot of the two different trajectories as functions of *Ca* and *Wi*. Treating the tension along the curved streamlines due to the non-zero first normal stress difference in the viscoelastic medium as an enhancement to the interfacial tension, we have developed an approximate force balance model for the zone of spiraling streamlines. It qualitatively captures the observed scaling of the critical *Ca* and *Wi* values at the phase boundary. The effects of unequal size, initial configuration, and non-unity viscosity ratio are briefly investigated. https://doi.org/10.1122/8.0000374

I. INTRODUCTION

Particle suspensions, both rigid and deformable, in Newtonian or non-Newtonian fluid, are omnipresent in many natural and industrial phenomena such as blood flow, microfluidics, cell sorting devices, chemical and material processing, food processing, the flow of slurries, oil and gas exploration, 3D printing, drilling muds, and paint industries [1–5]. Macroscopic rheological properties of these suspensions, i.e., the effective viscosity of the system, diffusion of particles, shear-thinning or thickening effects, depend on the microscopic behavior of particles such as their orientations, interparticle interactions, cross-stream migration, deformation, and the rheology of surrounding fluids [6–9]. Therefore, complex behaviors of a suspension or an emulsion can sometimes be understood by a single [10,11] or two-particle interactions [12–16]. Here, we study the pair interactions between two viscous drops in a viscoelastic medium in shear.

In most applications, owing to the small size and velocity, the flow is dominated by the inertialess Stokes flow. Due to the reversibility of the Stokes flow equation, a pair of perfect rigid spheres in shear follow their original streamlines after a collision [17]. Therefore, the particle separation mediated by hydrodynamic interactions or shear-induced diffusion in a rigid suspension cannot be explained by these reversible pair dynamics, unless some other mechanisms such as inertia, surface roughness, or viscoelasticity break the symmetry of the system [12,18,19]. Following the pioneering study of Batchelor and Green [20], several studies have explored solid particle interactions in Newtonian and non-Newtonian fluids elucidating the binary collision between rigid spheres in viscous and viscoelastic media under shear [12,19,21,22]. In the Stokes regime, a pair of rigid particles in a Newtonian fluid approach each other in shear, rotate together as a dumbbell, and separate along the original streamlines, except for very small initial stream-wise separation that can induce permanent doublet type of rotation due to the closed streamlines very near the particles [12,23]. On the other hand, rigid particles suspended in a viscoelastic medium, due to the broken symmetry, do not follow original streamlines after a collision, and particle trajectory is no more symmetric [19]. For particles passing each other in shear, post-collision cross-stream separation between particle centers decreases with the increase in surrounding fluid elasticity [22,24,25]. Here, one also encounters different types of trajectories: passing, tumbling, and return, depending on the initial cross-stream separation between particle centers, confinement, and elasticity of the surrounding fluid [12,24–26]. At low Weissenberg number (*Wi*), particles collide and pass each other (passing trajectory), but at higher *Wi* values, for small initial cross-stream separations, particles collide and rotate as a dumbbell (tumbling trajectory). Small initial separations and higher confinement ratios induce a returning type of trajectory, where particles come close to each other, collide, reverse, and return [26,27]. Increasing *Wi* increases the critical initial cross-stream separation distance between particle centers where the transition from tumbling trajectory to passing

[a)]Author to whom correspondence should be addressed: Sarkar@gwu.edu

trajectory occurs, which suggests that viscoelasticity induced normal stress differences keep the particles together even at larger initial separations [26]. Numerical simulations of effective rheology of viscoelastic suspension have found that particle interactions have significant effects on the overall effective rheology of viscoelastic suspensions [28,29]. Hwang *et al* [28] in their 2D simulation found clustering of two particles in Oldroyd-B matrix with tumbling trajectories and strong elongational flows between separating particles, the latter also found by smooth-particle hydrodynamics simulation of Vazquez-Quesada *et al* [29]. The signature of strong retarding stresses in extensional flows was also found in experimental investigations of extensional rheology of rigid sphere suspensions in a viscoelastic matrix [8,30].

In the case of drops, their deformability adds additional complexity [10,31,32]. It also breaks the reversibility of the Stokes flow. Since the first study of Taylor [33], there have been many investigations [6,34,35] of drops in Newtonian and non-Newtonian systems, especially in relation to microfluidics applications [36]. However, although drop-pair interactions in a viscous liquid have received some attention [35,37–40], their study in viscoelastic media is far from complete [6]. Drop deformation itself provides interesting phenomena absent for rigid particles, such as wall-induced lateral migration of a single drop [41,42]. There have been studies of inertia induced [38] and confinement-dominated reversed trajectories after binary collision [40,43] between viscous drops. Viscoelasticity introduces new physics, and unlike viscous flows, our intuition about viscoelastic flows is severely limited due to the presence of multiple forces and complex constitutive equations that defy simple explanations. Surrounding fluid viscoelasticity has nonmonotonic effects on drop deformation [35,44] and viscoelasticity can also influence wall-induced lateral migration [45,46] and alignment of particles [47,48]. Unlike pairwise interactions between rigid particles, interactions between drops, which are crucial to fully understand dilute or concentrated viscoelastic emulsions, have not been subjected to many investigations [6,7,9,12].

Here, we numerically study trajectories of two equal-sized viscous drops suspended in a modified Chilcott–Rallison [49,50] type viscoelastic fluid (also often called FENE-MCR) under steady free shear at negligible inertia. We study the relative trajectory between the drop centers in viscoelastic media. The main focus of this study is to understand the effect of drop deformability, capillary number, and surrounding fluid elasticity (*Wi*) on post-collision drop trajectories. In Secs. II and III, we describe briefly the mathematical formulation and problem setup. In Sec. IV, we describe our numerical results offering a qualitative explanation for the numerical observations. In the Appendix, we develop a simplified force balance model that captures the observed scaling behavior. Section V offers concluding remarks.

II. MATHEMATICAL FORMULATION AND NUMERICAL IMPLEMENTATION

The mathematical formulations underlying our computational study to simulate drops suspended in a viscoelastic matrix have been described in detail in our previous publications [32,44,45]. Here, we give a brief description for completeness. The complete drop-matrix system is governed by the incompressible momentum conservation equations in the entire domain Ω,

$$\frac{\partial(\rho\mathbf{u})}{\partial t}+\nabla\cdot(\rho\mathbf{u}\mathbf{u})=\nabla\cdot\boldsymbol{\tau}-\int_{\partial B} d\mathbf{x_B}\kappa\mathbf{n}\Gamma\delta(\mathbf{x}-\mathbf{x_B}), \tag{1}$$

$$\nabla\cdot\mathbf{u}=0. \tag{2}$$

The total stress $\boldsymbol{\tau}$ is decomposed into pressure, polymeric, and viscous parts,

$$\boldsymbol{\tau}=-p\mathbf{I}+\mathbf{T}^p+\mathbf{T}^v,\quad \mathbf{T}^v=\mu_s\mathbf{D}, \tag{3}$$

where p is the pressure, μ_s is the solvent viscosity, and $\mathbf{D}=(\nabla\mathbf{u})+(\nabla\mathbf{u})^T$ is twice the deformation rate tensor. The superscript T represents the transpose. $\mathbf{T}^p$ is the viscoelastic stress due to the presence of polymer. In Eq. (1), Γ is the interfacial tension (constant), ∂B represents the surface of the drop consisting of points $\mathbf{x}_B$, κ is the local curvature, $\mathbf{n}$ is the outward normal, and $\delta(\mathbf{x}-\mathbf{x}_B)$ is the three-dimensional Dirac delta function. The viscoelasticity of the surrounding fluid has been modeled by a modified Chilcott–Rallison type [49,50] constitutive equation (also called FENE-MCR) as in our recent computational studies [45,51]. Over the years, we adopted the simplest rate type constitutive equation for viscoelasticity with a single relaxation time, intending to understand the physics in simplest canonical situations. Our earlier studies used the Oldroyd-B model [32,44,52]. Unlike Oldroyd-B, FENE-CR and FENE-MCR models have a finite extensional viscosity. Like Oldroyd-B, they also have a constant shear viscosity. Both models have been extensively used to model different viscoelastic flows [53–56] (see a detailed discussion of their use in [45]). The FENE-CR [49] constitutive equation in terms of the conformation tensor $\mathbf{A}$ is given by

$$\frac{\partial\mathbf{A}}{\partial t}+\mathbf{u}\cdot\nabla\mathbf{A}=\nabla\mathbf{u}\cdot\mathbf{A}+\mathbf{A}\cdot(\nabla\mathbf{u})^T-\frac{f}{\lambda}(\mathbf{A}-\mathbf{I}). \tag{4}$$

The relation between the stress $\mathbf{T}^p$ and conformation tensor $\mathbf{A}$ is

$$\mathbf{A}=\left(\frac{\lambda}{\mu_p f}\right)\mathbf{T}^{\mathrm{p}}+\mathbf{I}. \tag{5}$$

Therefore, the stress constitutive equation becomes

$$\frac{\partial\mathbf{T}^p}{\partial t}+\{\mathbf{u}\cdot\nabla\mathbf{T}^p-\nabla\mathbf{u}\cdot\mathbf{T}^p-\mathbf{T}^p\cdot\nabla\mathbf{u}^T\}+f\,\mathbf{T}^p\left[\frac{\partial}{\partial t}\left(\frac{1}{f}\right)+\mathbf{u}\cdot\nabla\left(\frac{1}{f}\right)\right]+\frac{f}{\lambda}\mathbf{T}^p=\frac{f}{\lambda}\mu_p\mathbf{D}, \tag{6}$$

where

$$f = \frac{L^2 + \frac{\lambda}{\mu_p}(\sum T_{ii}^p)}{L^2 - 3}, \tag{7}$$

μ_p is the polymeric viscosity, λ is the relaxation time, and L is the finite extensibility, introduced by the FENE-CR model, which limits the maximum length of the end-to-end vector for the polymer molecule. In the limit of $L \to \infty$, we obtain the Oldroyd-B equation with $f \to 1$ in Eq. (7). We use $L = 20$, increasing which was shown to make little difference in the results [45]. Note that the FENE being a nonlinear modification does not affect the linear viscoelastic responses G' and G'' and results in a finite extensional viscosity in a uniaxial extension of strength $\dot{\gamma}$ for all Wi,

$$\mu_E = \frac{T_{xx} - T_{yy}}{\mu\dot{\gamma}} = 3 + f\beta\left(\frac{2}{f - 2Wi} + \frac{1}{f + Wi}\right). \tag{8}$$

In the limit of Oldroyd B, i.e., $L \to \infty$ or $f \to 1$, one notes the well-known singularity at $Wi = 0.5$, which is mitigated by the introduction of Eq. (7) that restricts f through $\sum T_{ii}^p$. Similar to Oldroyd B, the FENE-CR model results in a constant shear viscosity. The rheology of FENE-CR (i.e., its extensional viscosity and first normal stress difference as functions of the Wi) was provided by Oliveira [57].

The terms $f\,\mathbf{T}^p\left[\frac{\partial}{\partial t}\left(\frac{1}{f}\right) + \mathbf{u}\cdot\nabla\left(\frac{1}{f}\right)\right]$ are negligible in our simulations [50], and by dropping them we arrive at a modified FENE-CR equation,

$$\frac{\partial \mathbf{T}^p}{\partial t} + \{\mathbf{u}\cdot\nabla\mathbf{T}^p - \nabla\mathbf{u}\cdot\mathbf{T}^p - \mathbf{T}^p\cdot\nabla\mathbf{u}^T\} + \frac{f}{\lambda}\mathbf{T}^p = \frac{f}{\lambda}\mu_p\mathbf{D}. \tag{9}$$

By using the elastic and viscous stress splitting method used by [58], the viscoelastic stress can be expressed in the following form:

$$(\mathbf{T}^p)^{n+1} = [(\mathbf{T}^p)^n - (\mu_p\mathbf{D})^n]e^{-(f/\lambda)\Delta t} + (\mu_p\mathbf{D})^n - \frac{\lambda}{f}[\mathbf{u}\cdot\nabla\mathbf{T}^p - \nabla\mathbf{u}\cdot\mathbf{T}^p - \mathbf{T}^p\cdot\nabla\mathbf{u}^T]^n[1 - e^{-(f/\lambda)\Delta t}]. \tag{10}$$

The equations are solved in a Cartesian domain and the location of the drop is tracked with a front tracking method [59,60]. Equations (1) and (2) along with the viscoelastic constitutive equation (10) are solved by a semi-implicit finite difference projection method and an alternating direction implicit (ADI) scheme is applied to ease the restriction on the time step. A multigrid method is used to solve the pressure position equation. Details of the implementation of the above algorithm can be found in [32,45,61].

III. PROBLEM SETUP

Two equal-sized spherical drops of radius a are placed in a rectangular computational domain of sizes $L_x = 30a$, $L_y = 30a$, $L_z = 5a$ at $t = 0$ in an already setup shear flow (the effects of size difference have been studied in Sec. IV F). The computational domain is discretized with $384 \times 384 \times 64$ grid points. Initially, the drop centers are separated by a distance of Δx_0 and Δy_0 in the flow and cross-stream direction, respectively [Fig. 1(a)]. The drop centers are always in the same vorticity plane (x–z plane). In the y-direction, the top plate moves with a velocity U and the bottom plate with a velocity $-U$ obtaining a shear rate $\dot{\gamma} = 2U/L_y$. Periodic boundary conditions have been applied in the x and z directions. The imposed shear moves the upper (lower) drop in the positive (negative) x-direction. The drop radius a and the inverse shear rate $\dot{\gamma}^{-1}$ are used as the length and the time scales to define Reynolds number

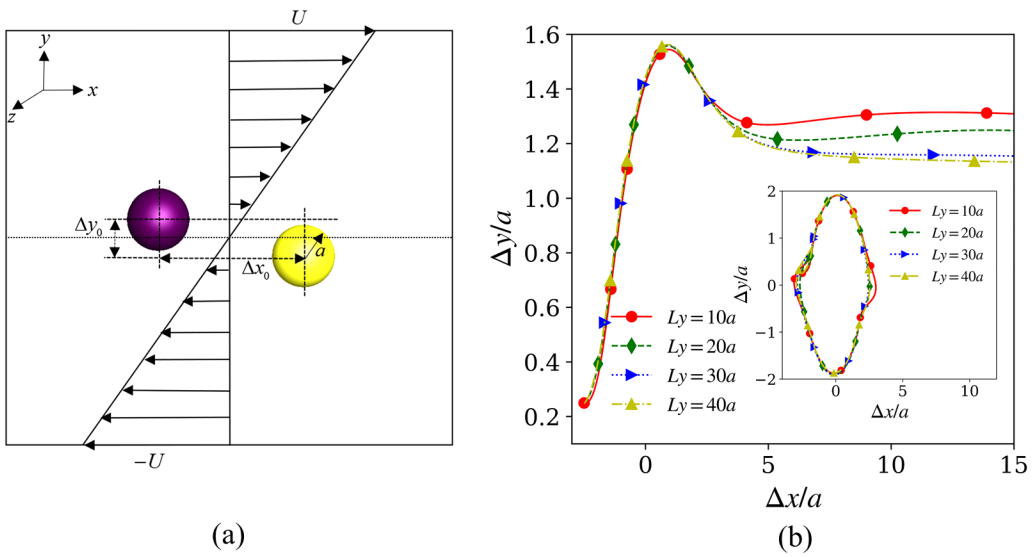

FIG. 1. (a) Schematic of the problem showing the initial separation of two drops in a shear flow. (b) Relative trajectory of pair of drops at $\Delta x_0 = 2.5a$, $\Delta y_0 = 0.25a$, $Ca = 0.2$ and $Wi = 0.5$ in different computational domain sizes in the gradient direction. The inset shows the same for $Ca = 0.01$ and $Wi = 2.0$.

$Re = \rho_m \dot{\gamma} a^2/\mu_m$, Capillary number $Ca = \mu_m \dot{\gamma} a/\Gamma$, and Weissenberg number $Wi = \lambda\dot{\gamma}$. The viscosity ratio is $\lambda_\mu = \mu_d/\mu_m$, density ratio $\lambda_\rho = \rho_d/\rho_m$, and polymeric to total matrix viscosity ratio $\beta = \mu_{pm}/\mu_m$. Subscripts m and d denote fluid and drop phases, respectively. The total viscosity of the surrounding fluid μ_m comprises the polymeric and the solvent viscosities $\mu_m = \mu_{sm} + \mu_{pm}$. All simulations assume $\lambda_\rho = 1.0$ and $\beta = 0.5$. While performing most simulations for $\lambda_\mu = 1.0$, Sec. IV E investigates the effects of viscosity ratio variation. The initial separations between drops are kept constant at $\Delta x_0 = 2.5a$, $\Delta y_0 = 0.25a$ and $\Delta z_0 = 0$, except when we study the effects of the initial drop separation. Re has been kept at 0.01 to achieve a flow close to the Stokes flow. The above code was run with the help of XSEDE's computational resources [62].

IV. RESULTS AND DISCUSSION

A. Effect of domain size

Investigation toward the viscoelastic code validation and its convergence can be found in our previous works [32,45]. Note that here we study drop interactions in an unconfined flow. However, the computational domain is subjected to periodic boundary conditions in the flow (x) and the vorticity (z) directions and wall boundary conditions in the gradient direction, the latter to generate the shear flow. The presence of walls could significantly alter the results if the domain is not large enough [26,40]. The domain effects have been studied in detail in our previous publications on pair interactions in viscous media, indicating that $L_x = 30a$, $L_y = 30a$, and $L_z = 5a$ are sufficient for avoiding the boundary effects [63], when the drops/particles are placed in the central plane. Here, we briefly investigate the confining effects of the walls on the relative drop trajectory [Fig. 1(b)] for four different L_y and two different sets of Ca and Wi (one for passing trajectory and the other for tumbling). The change in the relative trajectory of the drops as we go from $L_y = 30a$ to $L_y = 40a$ is insignificant confirming that $L_y \sim 30a$ is sufficient to avoid confinement effects. We have previously investigated the effects of grid size for the pair-collision problem [38] indicating that the size $384 \times 384 \times 64$ is more than sufficient for our purpose. Comparison with previous experiments [13] and numerical solutions [63] offers confidence about the capabilities of the code to adequately resolve the deforming drops.

B. Effects of matrix viscoelasticity and drop deformability

In this section, we discuss the effects of surrounding fluid elasticity and drop deformability on the cross-stream separation between drops by varying Wi from 0.0 to 2.0 and Ca from 0.01 to 0.2. At $Ca = 0.01$, drop deformation is minimal while at $Ca = 0.2$, drop in a steady shear attains an approximately ellipsoidal shape [32,33,44].

In Fig. 2, we consider the relative trajectory between drops at $Ca = 0.2$ as a case of a highly deformable drop for different Wi of the suspending medium. As noted, we used initial drop separation to be fixed at $\Delta x_0 = 2.5a$ and $\Delta y_0 = 0.25a$ for all simulations. All cases led to drops passing each other. Figure 2(a) shows the time evolution for the case of $Wi = 2.0$ plotting the cross-stream separation as a function of time. As was seen in our previous investigation of a viscous system [38], drop interactions have a signature footprint—first approach each other (zone 1), then collide in the compressional quadrant (zone 2), interact in the extensional quadrant before separating (zone 4) and separate (zone 5) (see Fig. 2, Multimedia view, for a movie of the trajectory). We were able to successfully match with experimentally observed evolution of drop deformation, drop inclination, separation, and relative inclination between drops [13,38]. In Fig. 2(b), we plot the cross-stream separation as a function of flow-wise separation for different Wi. Note that unlike a rigid particle pair in a Newtonian medium, the post-collision cross-stream separation is larger than its initial value even for the Newtonian case ($Wi = 0$) [17]. The symmetry under flow reversal is broken due to the nonlinearity (the interface conditions on a moving boundary) introduced by the drop deformation. Loewenberg and Hinch [37] simulated this

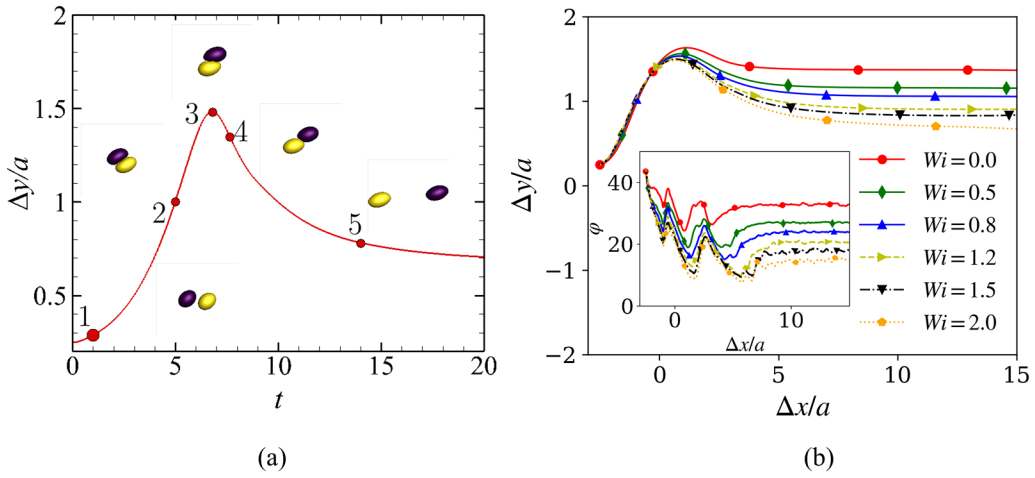

FIG. 2. (a) Drop interaction snapshots at different simulation times along with their cross-stream separation with $\Delta x_0 = 2.5a$ and $\Delta y_0 = 0.25a$ at $Wi = 2.0$ and $Ca = 0.2$. (b) Relative trajectory of the same pair of drops for different Wi values. Inset shows drop inclination with the flow for the same Wi values. Multimedia view: https://doi.org/10.1122/8.0000374.1

phenomenon in a viscous system using a boundary element method and investigated the self-diffusion of viscous drops in viscous media. In a previous article, we successfully compared their results as well as those of others [14]. With increasing Wi, the final post-collision Δy decreases, which can be explained by noting that the drop inclination (the angle between the semi-major axis of the deformed drop, approximated as an ellipsoid, and the flow direction) decreases with increasing medium viscoelasticity [the inset of Fig. 2(b)]. The matrix elasticity aligns the drop with the flow due to the first normal stress differences, as we also saw in the case of a single drop in a viscoelastic medium under shear [44]. In a drop-pair interaction, the inclination, even in a viscous system, has been shown by both experiment and matching computation to display a complex evolution [13,38] with multiple maxima and minima. Initially, in the approach phase, the drop deforms due to the shear and inclination decreases, reaching a minimum when the drops are close to each other, then they press and rotate together as a dumbbell and separate reaching a second maximum while separating [Fig. 2(b), inset]. But overall increasing Wi decreases inclination resulting in drops passing more easily leading to lower final cross-stream separation.

When the drops are less deformable, i.e., at lower capillary numbers, they behave differently and display a new type of trajectory—tumbling. Figure 3(a) shows the time evolution for the case of $Wi = 2.0$ and $Ca = 0.01$ plotting the cross-stream separation as a function of time. The drops after collision fail to separate and continue to rotate leading to a negative cross-stream separation (see Fig. 3, Multimedia view, for a movie of the trajectory). We can see two peaks (zone 3 and zone 6) while the drops come on top of each other. Such tumbling/rotating trajectory was also observed experimentally [23] as well as numerically [24–28] for shear-induced pair interactions between rigid spheres in a viscoelastic medium above a critical Wi. Figure 3(b) shows drop interaction at different Wi for the same $Ca = 0.01$. It shows passing trajectories at the lower three values of Wi, and tumbling at $Wi = 1.2$, 1.5, and 2.0. Such tumbling was observed for rigid particle pairs in a viscous fluid [23] only for very close initial separation. However, investigation of drop-pair collision in a viscous system did not display tumbling trajectories [37]. This can be ascribed to the no-slip conditions resulting in greater resistance in the lubrication layer between rigid spheres compared to deformable drops. During the transition from passing to tumbling trajectory for intermediate values of $Wi = 1.2$ [Fig. 3(b)], the rotating drop centers move back and forth in the flow direction transiently increasing their horizontal separation. For rigid particle pairs in viscoelastic media, similar back and forth motion was also seen during transitioning from passing to tumbling [24]. Note that due to the symmetry of the original problem, i.e., the symmetry of the imposed shear flow and the symmetrical positions of the drops above and below the symmetry plane, the relative cross-stream displacement $\Delta y = y_{\text{top drop}} - y_{\text{bottom drop}} = 2y_{\text{top drop}}$. This symmetry of the problem renders the tumbling trajectory, i.e., two drops rotating around each other, symmetric across the zero relative cross-stream separation line, crossing it when $y_{\text{top drop}} = 0$ [Fig. 3(b)], unlike in the case of passing trajectories [Fig. 2(b)].

Figures 4(a) and 4(b) plot the post-collision cross-stream separation between drops undergoing passing trajectories as a function of Wi and Ca after the drops reached a steady cross-stream separation. We refer to it as the final separation $(\Delta y)_f/a$. The curves are stopped when the parameters reach the region of tumbling trajectories, where there is no such final cross-stream separation. For a given Ca, increasing fluid viscoelasticity, i.e., increasing Wi, leads to lower final cross-stream separations $(\Delta y)_f/a$, eventually leading to tumbling trajectories for lower Ca cases [Fig. 4(a)]. Similarly, for a given Wi, lowering Ca eventually leads to tumbling trajectories [Fig. 4(b)]. For the range of Wi considered ($Wi \leq 2$), drops for Ca greater than or equal to 0.1 do not show tumbling trajectory. However, less deformable drops at $Ca = 0.05$ and below show tumbling trajectories at higher viscoelasticity. In both Figs. 4(a) and 4(b), we notice zig-zag variations in the final cross-stream separation with Wi and Ca, especially for the small Ca ($Ca \leq 0.05$) cases. To further investigate this variation, we chose the case of $Wi = 0.8$ with such a variation between $Ca = 0.01$ and $Ca = 0.05$ and plot in Figs. 4(c) and 4(d) the relative positions $(\Delta x)/a$ and $(\Delta y)/a$

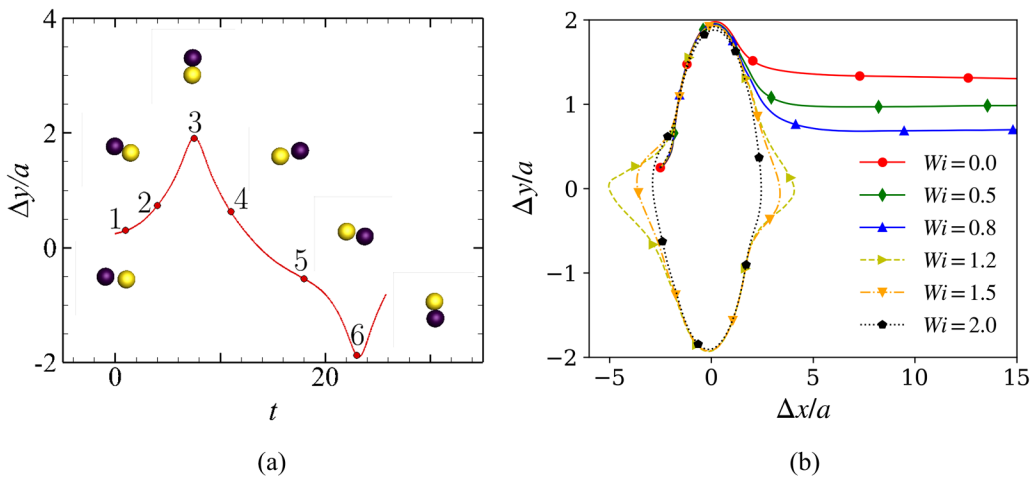

FIG. 3. (a) Drop interaction snapshots at different simulation times along with their cross-stream separation with $\Delta x_0 = 2.5a$ and $\Delta y_0 = 0.25a$ at $Wi = 2.0$ and $Ca = 0.01$. (b) Relative trajectories of the same pair of drops at different Wi. Multimedia view: https://doi.org/10.1122/8.0000374.2

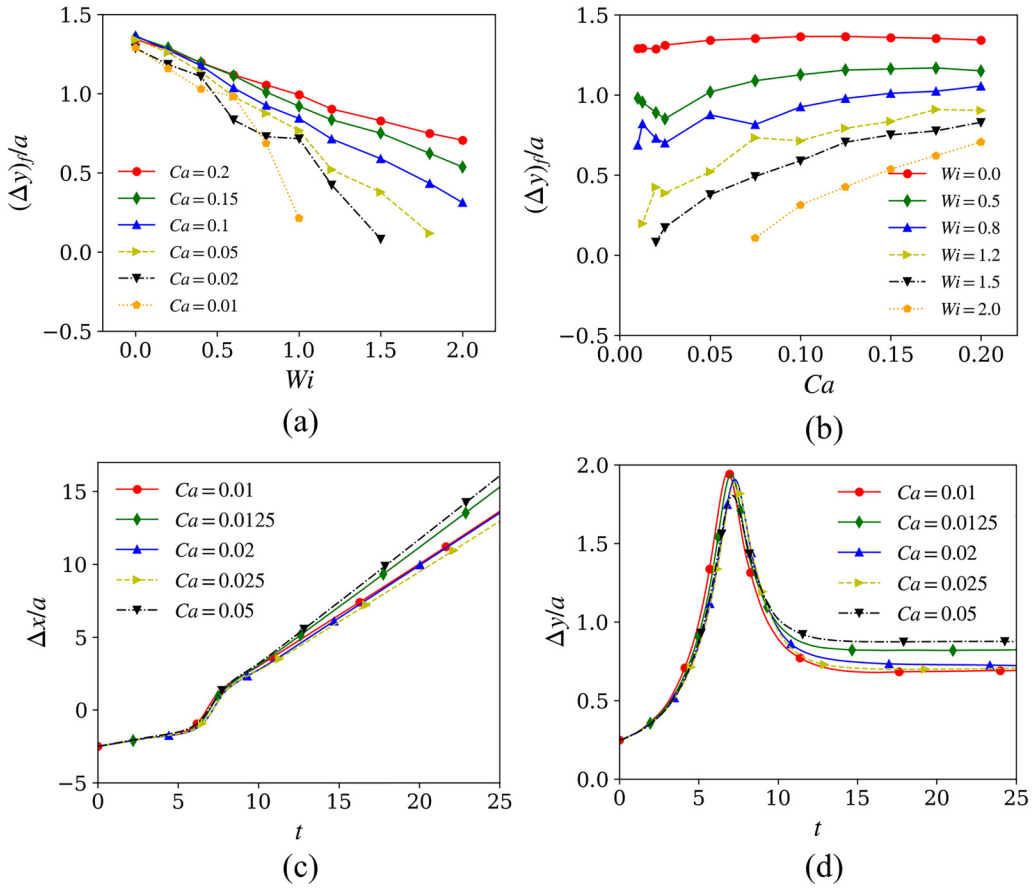

FIG. 4. Final cross-stream separation between drop centers as a function of (a) *Wi* and (b) *Ca* for passing trajectories. (c) and (d) show the relative position between drop centers in the flow and cross-stream directions, respectively, as a function of time at $Wi = 0.8$.

showing them to be smooth functions of time. However, the curves for different *Ca* values post-collision cross. A possible reason could be the dual competing effects of variation of *Ca*—increased *Ca* results in increased deformation but slower relaxation, *Ca* being the timescale $\mu_m a/\Gamma$ nondimensionalized by $\dot{\gamma}$. While typically increased *Ca* leads to larger deformation and thereby larger $(\Delta y)_f/a$, the slow relaxation of the drop shape post-collision could trigger a different trajectory. On the other hand, we note that for the small *Ca* cases the overall deformation is quite small, and the code uses a diffuse interface to represent the drop shape and find the drop position, which might numerically lead to the zig-zag variation.

C. Physics of transition between trajectories and phase plot in *Ca-Wi*

To understand the physics underlying the two types of trajectories, we plot in Fig. 5 streamlines around a single drop in a Newtonian ($Wi = 0.0$) fluid and a viscoelastic fluid each for two capillary numbers $Ca = 0.01$ and $Ca = 0.2$. For the two Newtonian cases [Figs. 5(a) and 5(b)], the streamlines are similar—curved spiraling streamlines very close to the drop and passing streamlines in the rest of the domain. In a pair interaction, the streamlines induced by one drop influence the motion of the other drop and lead to a passing trajectory. The small region of curved streamlines is too close to the drop to trigger tumbling trajectory for any of the Newtonian cases. On the other hand, at $Wi = 2.0$, Figs. 5(c) and 5(d) show a region of spiraling streamlines extending fore and aft of the drop. For the more deformable case ($Ca = 0.2$), the region is small in extent in the velocity gradient direction to trap the second drop in pair interaction; it leads to passing trajectory. But for $Ca = 0.01$, the largely undeformed drop induces spiraling streamlines around it which facilitates trapping the second drop into a tumbling trajectory. Thus, only lower *Ca* and higher *Wi* support tumbling trajectories in a pair interaction. Note that the spiraling streamline pattern has been predicted analytically [64] as well as observed numerically around a rigid sphere in viscoelastic fluid.[65] Their spiraling nature can best be understood as resulting from structural instability of the closed streamline region near a sphere in a reversible linear Stokes flow of Newtonian fluid. The closed streamline pattern can be broken by any one of the symmetry-breaking nonlinearities such as inertia [66,67], viscoelasticity [64], or deformation [68]. These effects distort the close streamlines of the Newtonian Stokes flow into spiraling streamlines. The exact topology is determined by a delicate balance between the new force, e.g., centrifugal, or normal stresses around the curved streamlines, and the viscous force. Subramanian and Koch [64] performed a perturbative analysis for a shear flow around a sphere in a second-order fluid to show this transition from closed to spiraling streamlines, which, in turn, results in an enhanced heat transfer from the sphere.

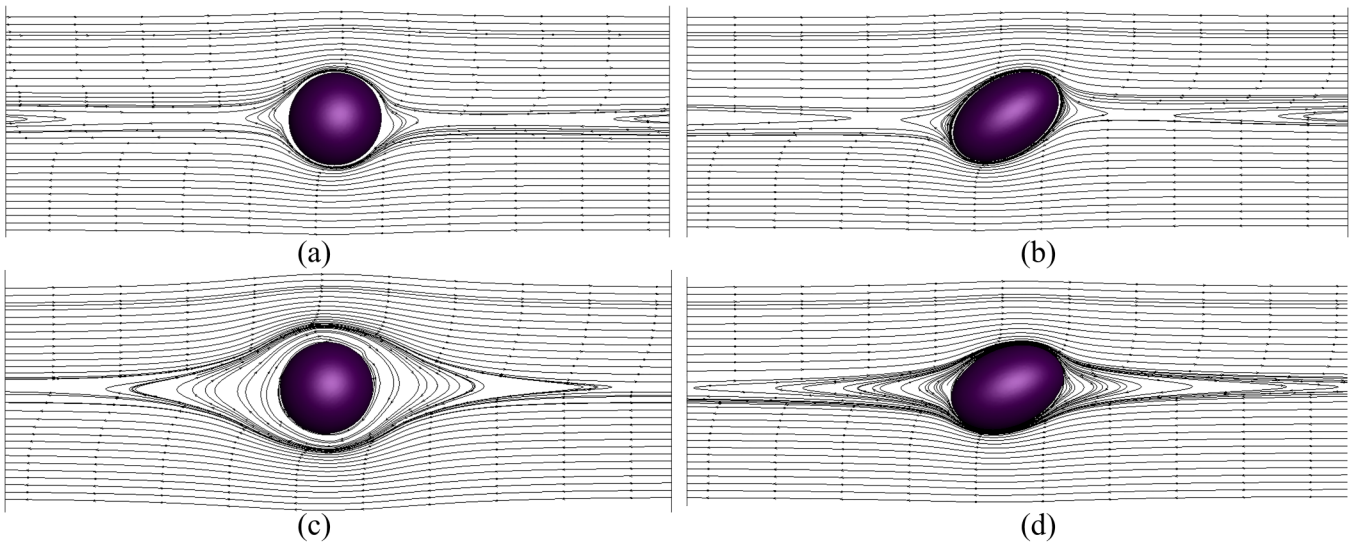

FIG. 5. Streamlines around a single drop placed at the center of the domain and at (a) $Ca = 0.01$, $Wi = 0.0$, (b) $Ca = 0.2$, $Wi = 0.0$, (c) $Ca = 0.01$, $Wi = 2.0$, and (d) $Ca = 0.2$, $Wi = 2.0$.

Apart from the changed streamline topology around a single drop due to viscoelasticity, pair interactions are also affected by the dynamic evolution of the polymeric stresses as the drops approach each other. Following Hwang *et al.* [28] and Vazquez-Quesada *et al* [29], we plot the trace of the conformation tensor A [see Eq. (5)] for two cases—one passing ($Wi = 2.0$, $Ca = 0.2$) and one tumbling ($Wi = 2.0$, $Ca = 0.01$)—at three different instants in Fig. 6. For the passing trajectory (top panel in Fig. 6), during compression, we notice the increased polymeric stresses near the drop tip as was also seen before in our single drop computation (Fig. 7 in [44]). However, as the drops separate, the squeeze-film flow between them during compression transitions to an extensional flow. It leads to a string-like region of high polymeric stresses connecting drops during their separation, also seen in computational simulation of multiple spheres suspended in an Oldroyd matrix [28,29]. Vazquez-Quesada *et al* [29]. saw such regions of large polymer stress connecting several particles even at a low volume fraction of 5%. They indicated that such regions of high polymer stresses at high *Wi* can give rise to shear thickening seen even at 0.5% in numerical simulations by Yang and Shaqfeh [69]. For a low *Ca* of 0.01 and the same high value of $Wi = 2.0$ (bottom panel of Fig. 6), the region of high polymeric stress surrounds the less deformed drop. Note that experimental investigation of a uniaxial elongational flow of a rigid sphere suspension in a viscoelastic matrix indicated an exponential increase in stresses with a strain that was modeled by an Oldroyd-B relation indicating the same underlying physics at the level of individual particle separation [30]. As shown in the Appendix, the perturbation flow field due to the presence of the viscosity-matched drop possesses an extensional component contributed by the interfacial tension that retards its deformation [see the velocity expression (A4) in the Appendix which decreases with increasing *Ca*]. The polymeric stresses are enhanced in the extensional flow, in turn impeding the drop separation. Higher *Ca*, i.e., lower interfacial tension gives rise to a weaker extensional component, warranting higher values of *Wi* and higher polymeric stresses to trap the drops in a tumbling trajectory.

Figure 7 shows a phase plot in *Ca*-*Wi* space indicating two types of trajectories as a function of *Ca* and *Wi*. As discussed above, tumbling trajectories occur for less flexible (small *Ca*) drops in a more viscoelastic matrix (large *Wi*). We do not see tumbling for $Ca = 0.075$ and above for any value

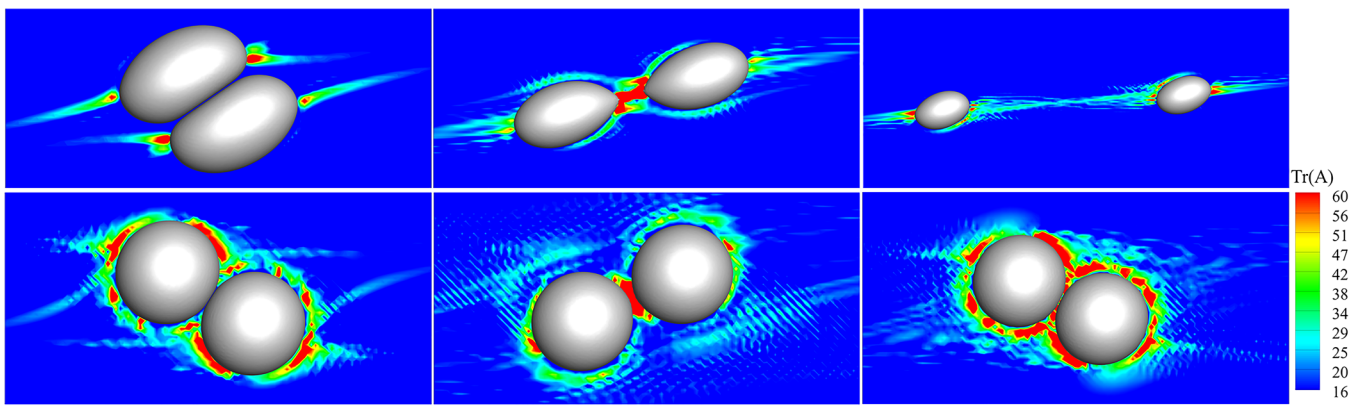

FIG. 6. The trace of the conformation tensor at three instants for a passing trajectory case $Ca = 0.2$, $Wi = 2.0$ (top panel) and a tumbling trajectory case $Ca = 0.01$, $Wi = 2.0$ (bottom panel).

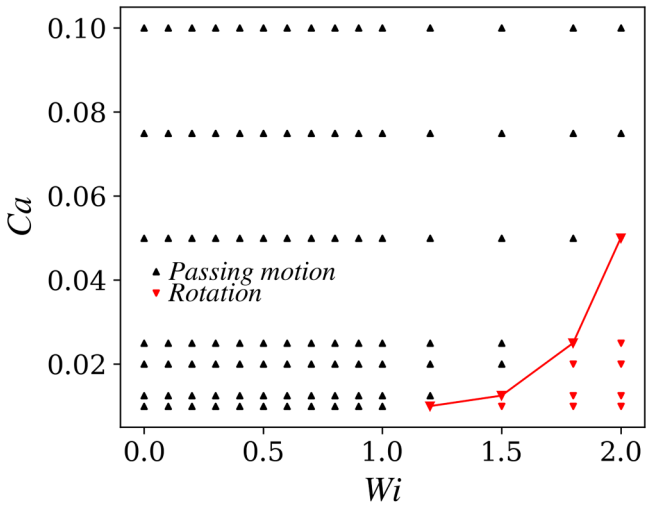

FIG. 7. Phase plot of types of trajectories as a function of *Ca* and *Wi*.

of *Wi* investigated here. For very high *Ca* values, the drop deformation also becomes unbounded leading to a breakup. Previously, we have shown that higher matrix viscoelasticity eventually enhances deformation and breakup [44]. The tumbling trajectory results from the increased zone of spiraling streamlines seen around a single drop in shear (Fig. 5), as well as the enhanced polymeric stresses in the region separating the interacting drops (Fig. 6).

Unlike a Newtonian system, obtaining a physical understanding of the phenomena in a viscoelastic system is difficult. The flow field governed by a system of partial differential equations and complex constitutive equations does not offer simple explanations. In the Appendix, we have developed a simplified theory of the linear dimension of the region of spiraling streamlines around a single drop as a function of *Wi* and *Ca*. It offers an understanding of the underlying physics of the force balance between the interfacial tension and the viscoelastic effects curving the streamlines away from their imposed shear-induced rectilinear form around a drop. The condition that the radius of the region of the spiraling streamline must be sufficiently large to trap the second drop results in an approximate quadratic scaling of $Ca_{critical}$ with *Wi* seen in Fig. 7.

D. Effects of initial cross-stream separation in the gradient and the vorticity directions

A large initial cross-stream separation would evidently lead to a passing trajectory. Above, we choose to restrict the investigation to $\Delta y_0/a = 0.25$. In this section, we vary this quantity $\Delta y_0/a < 1.0$ to examine its effects on the trajectory type. Figure 8(a) shows relative trajectories of drop centers at

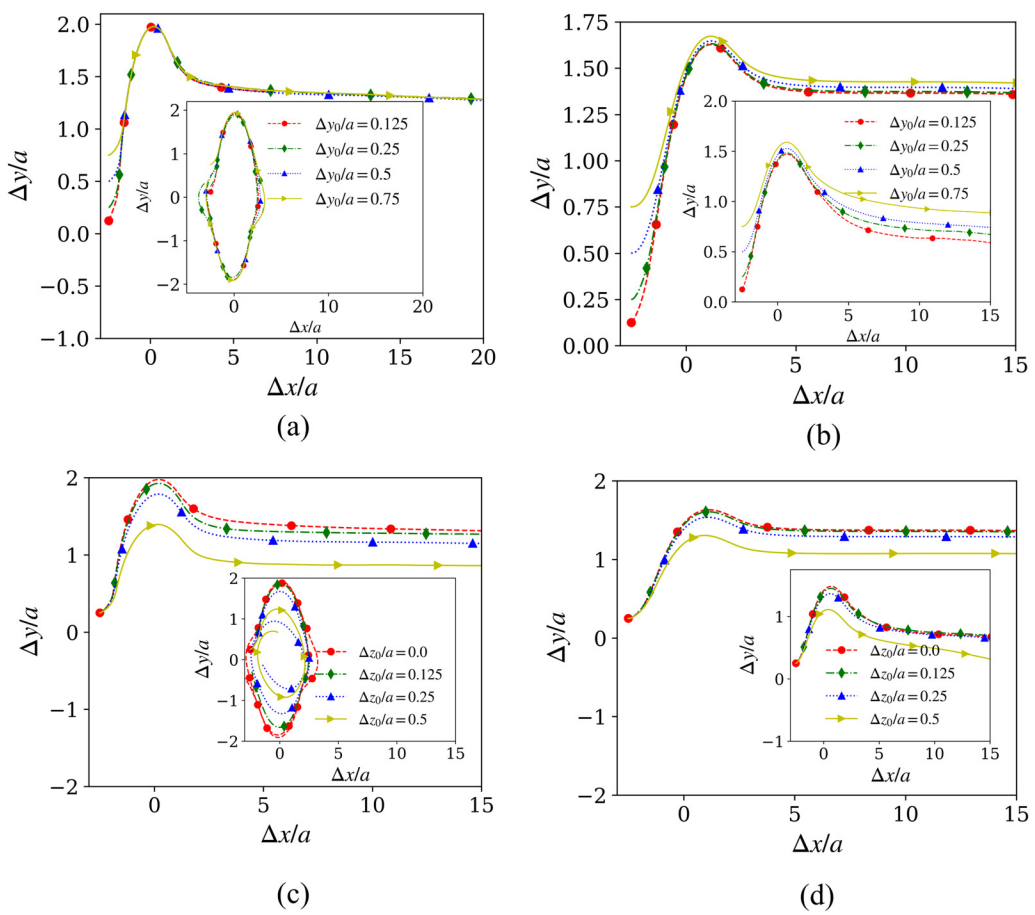

FIG. 8. Relative trajectory of drops at different initial cross-stream separations in the velocity gradient direction $\Delta y_0/a$ (all at $\Delta z_0/a = 0$) (a) $Ca = 0.01$ and $Wi = 0.0$ (inset: $Ca = 0.01$, $Wi = 2.0$); (b) $Ca = 0.2$ and $Wi = 0.0$ (inset: $Ca = 0.2$, $Wi = 2.0$) and different initial cross-stream separation in the vorticity direction $\Delta z_0/a$ (all at $\Delta y_0/a = 0.25$); (c) $Ca = 0.01$ and $Wi = 0.0$ (inset: $Ca = 0.01$, $Wi = 2.0$); (d) $Ca = 0.2$ and $Wi = 0.0$ (inset: $Ca = 0.2$, $Wi = 2.0$).

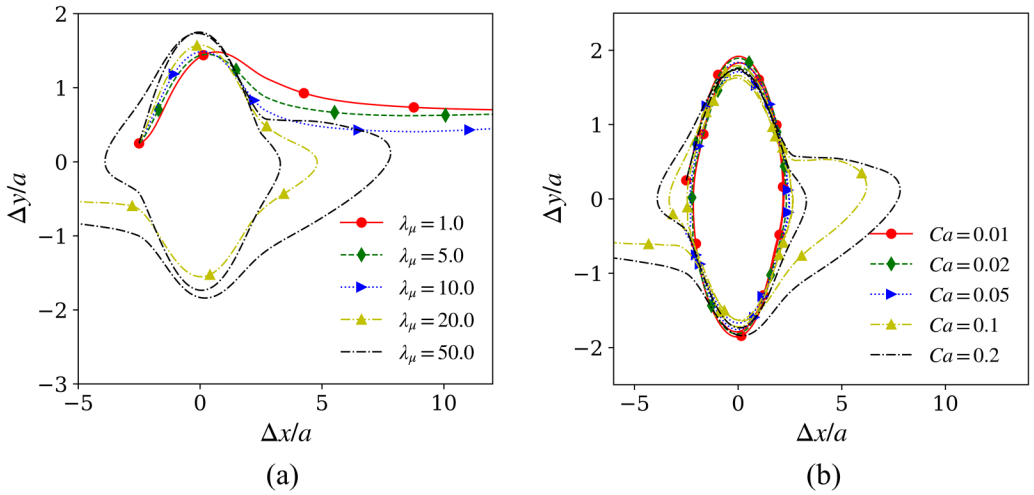

FIG. 9. (a) Relative trajectories of interacting drops with $Ca = 0.2$, $Wi = 2.0$ for different viscosity ratios λ_μ. Increasing λ_μ transitions passing trajectories into partially tumbling ones. (b) Relative trajectories of interacting drops with $\lambda_\mu = 50$, $Wi = 2.0$ for different Ca. Increasing Ca transitions tumbling trajectories into partially tumbling ones.

$Ca = 0.01$ for two different fluid conditions $Wi = 0.0$ and $Wi = 2.0$ (inset). The variation in $\Delta y_0/a$ does not change trajectory types, passing for $Wi = 0.0$ and tumbling for $Wi = 2.0$. At $Wi = 0.0$, all $\Delta y_0/a$ led to the same post-collision separation. As noted above, the results can be understood from the streamline pattern around a single drop (Fig. 5) that induces the trajectory in pair interactions. At $Wi = 2.0$, even with the $\Delta y_0/a$ change, the region of spiraling streamlines around them proved large enough to trap drops into tumbling trajectories. However, note that the largest one $\Delta y_0/a = 0.75$ led to small back and forth motion in the tumbling trajectory unlike at smaller $\Delta y_0/a$ values. At $Ca = 0.2$, passing trajectories are seen for all $\Delta y_0/a$ for $Wi = 0.0$ [Fig. 8(b)] and $Wi = 2.0$ [Fig. 8(b), inset]. For both Weissenberg numbers, post-collision final cross-stream separation $\Delta y_f/a$ increases with increasing $\Delta y_0/a$, the effects being more prominent for the viscoelastic case, in conformity with the understanding that matrix viscoelasticity reduces cross-stream separation, and drops tend to recover most of their initial cross-stream separation. In Figs. 8(c) and 8(d), we explore the effects of initial offset in the vorticity direction $\Delta z_0/a$ for the same set of Ca and Wi values. For the passing trajectories, increasing $\Delta z_0/a$ predictably leads to smaller $\Delta y_f/a$ with sliding interactions between drops. For the tumbling trajectories [inset of Fig. 8(c)], the circular orbits become smaller with increasing $\Delta z_0/a$. For the largest two $\Delta z_0/a$, we also note spiraling of the trajectories in conformity with the spiraling streamlines in a flow around a single drop noted as well as in the literature [64].

E. Effects of viscosity ratio variation

All simulations in other subsections (Secs. IV A–IV D and IV F) are limited to the viscosity matched case. Increasing the viscosity ratio decreases the deformation reaching rigid spheres in the limit of $\lambda_\mu \to \infty$. Figure 9(a) shows that increasing viscosity ratio, with all other parameters kept the same ($Ca = 0.2$, $Wi = 2.0$), a passing trajectory for $\lambda_\mu = 1$ transitions to partially tumbling but eventually separating trajectories. The cases with $\lambda_\mu = 5$ and 10 show passing trajectories with final cross-stream separation $\Delta y_f/a$

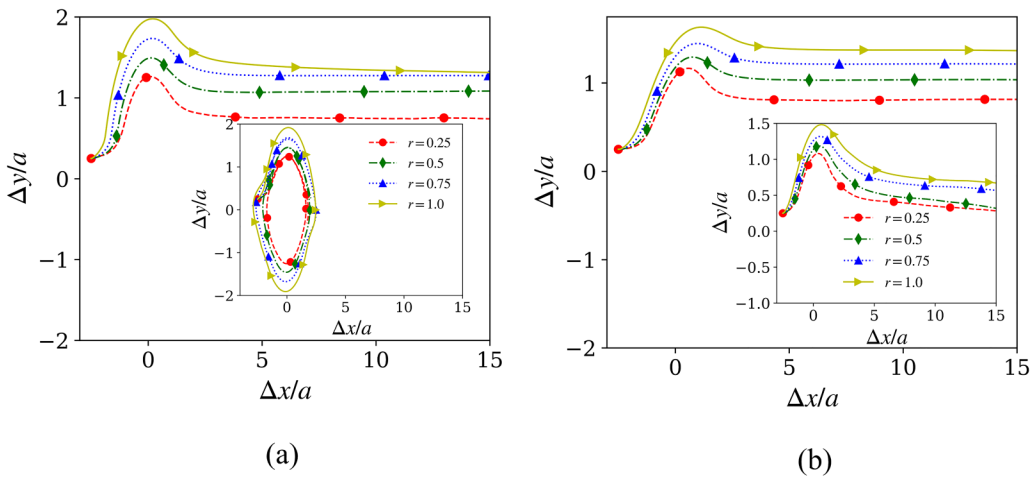

FIG. 10. (a) Relative trajectories of interacting drops with $Ca = 0.01$ and $Wi = 0.0$ (inset $Wi = 2.0$) for different initial radius ratios (r) of the drops. (b) The same as in (a) but for $Ca = 0.2$.

progressively decreasing with the viscosity ratio. For the highest viscosity ratios $\lambda_\mu = 20$ and 50, one obtains trajectories that tumbled once ($\lambda_\mu = 20$) or twice ($\lambda_\mu = 50$) and then separated from each other. Figure 9(b) further investigates the highest viscosity ratio $\lambda_\mu = 50$. As the capillary number is decreased, the partially tumbling trajectories at $Ca = 0.2$ in Fig. 9(a) become fully tumbling, closed and symmetric, at and below $Ca = 0.05$.

F. Effects of unequal drops

Finally, in this section, we briefly study the case of unequal sizes for the drops. With all the parameters the same, i.e., $\Delta x_0 = 2.5a$, $\Delta y_0 = 0.25a$, we use two drops with initial radii a and ra and vary the radius ratio r. We choose two sets of Weissenberg number and capillary number, $Wi = 0.0$ and 2.0 and $Ca = 0.01$ and 0.2. Figure 10(a) investigates the case of a small capillary number $Ca = 0.01$—in the main figure ($Wi = 0.0$), we notice that all radius ratios lead to passing trajectories, but decreasing r leads, as expected, to decreased hindrance (smaller scattering cross sections) and therefore smaller final cross-stream displacements $\Delta y_f/a$. In the inset of Fig. 10(a), the same variations for the same capillary number but for the $Wi = 2.0$ leads to tumbling trajectories, with more different drops tumbling with tighter orbits. Figure 10(b) investigates the dynamics for $Ca = 0.2$ with $Wi = 0.0$ in the main plot and $Wi = 2.0$ in the inset. It shows passing trajectories for all cases at this larger capillary number with similar variations with varying radius ratios, i.e., decreasing final cross-stream displacements $\Delta y_f/a$ with decreasing radius ratios.

V. CONCLUSION

We investigated shear-induced pair interactions between two equal-sized Newtonian drops suspended in a viscoelastic (modified FENE-CR) medium varying the Capillary number (Ca) and the Weissenberg number (Wi). The matrix viscoelasticity introduces a tumbling trajectory—drops form a bound pair and rotate—in addition to the usual passing trajectory one sees in a Newtonian system. For the passing trajectories, while the increasing capillary number expectedly increases final relative cross-stream separation, increasing matrix viscoelasticity decreases it indicating reduced diffusion of droplets in a viscoelastic medium. The tumbling trajectories, also predicted numerically in pair interactions between rigid spheres in a viscoelastic medium, are only seen at low Ca and high Wi. With simulations sweeping the parameter space, we show a phase plot separating the two types of trajectories in Ca-Wi space indicating a critical Wi below which there is no tumbling trajectory and an approximate quadratic relationship between the variables at the phase boundary between the two trajectories. Slight variations in initial separation in the cross-stream gradient direction are shown to not influence the type of post-collision trajectory. Initial separations in the vorticity direction and decreasing the radius ratio between drops decreases interactions leading to smaller final cross-stream displacement as expected. An increase in the viscosity ratio leads to a transition toward tumbling trajectories. The tumbling trajectory is discussed to result from the zone of spiraling streamlines around the drop, which, in turn, are caused by the tension along the curved streamlines. An approximate force balance model has been developed that treats the tension due to the first normal stress difference in a manner analogous to the interfacial tension. It shows that the disturbance field due to the drop created by these tensions acts against the rectilinear imposed shear to give rise to a sufficiently large zone of curved streamlines to trap an approaching drop into a tumbling trajectory. The model captures the scaling between critical Wi and Ca determining the transition between passing trajectories at high Ca and low Wi to tumbling trajectories at low Ca and high Wi. We note that the present investigation does not account for possible coalescence, which is driven by nonhydrodynamic (e.g., van der Waals) forces not included in the modeling. Colliding drops at contact form a thin film between them, which needs to drain sufficiently under the external flow before it can rupture to coalescence [70]. In a shear-induced drop interaction, the drops experience a glancing collision [71]; in a Newtonian passing trajectory, they push against each other at the compression quadrant before pulling away from each other in the extension quadrant, often leading to less time for drainage [72]. In a polydimethylsiloxane (PDMS)–polyisobutylene (PIB) binary system, the coalescence was seen to be extremely rare and only seen when PIB was used as the dispersed phase and PDMS as matrix [13] in the extension quadrant. However, for a tumbling trajectory indicated here in a viscoelastic system, the drops remain in contact for a long time that might induce coalescence. Experimental investigations will be needed to verify the simulated predictions as well as such possible phenomena.

ACKNOWLEDGMENTS

K.S. acknowledges partial support from The George Washington University (GWU) and National Science Foundation under Award No. 2019507. The authors acknowledge time on the Pegasus cluster at GWU. K.S. thanks Professor Bill Schowalter for reading a draft and offering his insight. The computation was also performed using the Comet cluster at the San Diego Supercomputer Center, through the Extreme Science and Engineering Discovery Environment (XSEDE) program [62], which is supported by the National Science Foundation under Grant No. ACI-1548562 (CTS180042).

AUTHOR DECLARATIONS

Conflict of Interest

The authors have no conflict of interest.

Author Contributions

X.P. and Y.T. contributed equally to this work.

APPENDIX: Physical model for the transition between trajectories

In the following, we attempt physical reasoning behind the zone of spiraling streamlines $\Lambda \sim r \in (a, R_{\text{spiral}})$ based

on the local flow and a force balance underlying the physics that the tension around the streamlines in a viscoelastic fluid near a drop (which is mostly spherical at small capillary numbers) gives rise to curved circular streamlines. Note that in a purely viscous case, a viscosity matched drop placed in a shear flow introduces a velocity field that changes the rectilinear shear flow into a flow field with curved streamlines around the drop. The imposed linear shear flow is a superposition of equal extension and rotation. The rotation is not disturbed by the drop that would rotate with the same rate as that of the imposed shear, but the interfacial tension working against drop deformation introduces an opposing extension flow to satisfy the boundary conditions at the interface. This is easily seen in the perturbative analytical expression for the deformation of a drop $D = (16 + 19\lambda)/16(\lambda + 1)Ca$, where $D = (L - B)/L + B)$, with L and B being the major and the minor axes of an ellipsoid approximately describing the drop shape [73]. $D \sim Ca$ denotes the balance between the surface tension-induced pressure difference with the imposed shear.

To see how the extensional disturbance flow is driven by Ca, we use a Green's function formulation of the Stokes problem inside and outside the drop and obtain an exact expression for the velocity field outside the drop as a sum of the imposed field $\mathbf{u}^{\infty}(\mathbf{x})$ and a perturbation due to the drop $\mathbf{u}^{d}(\mathbf{x})$,

$$u_j(\mathbf{x}) = u_j^{\infty}(\mathbf{x}) + u_j^{d}(\mathbf{x}) = u_j^{\infty}(\mathbf{x}) - \frac{1}{8\pi\mu}\int_{A_d} \Delta f_i(\mathbf{y}) G_{ij}(\mathbf{x}, \mathbf{y}) dA(\mathbf{y}),$$

$$G_{ij}(\mathbf{x}, \mathbf{y}) = \frac{\delta_{ij}}{|\mathbf{x} - \mathbf{y}|} + \frac{(x_i - y_i)(x_j - y_j)}{|\mathbf{x} - \mathbf{y}|^3}, \tag{A1}$$

$$\Delta\mathbf{f} = (\mathbf{f} - \tilde{\mathbf{f}}) = \Gamma(\nabla \cdot \mathbf{n})\mathbf{n},$$

where $G_{ij}(\mathbf{x}, \mathbf{y})$ is the free space Stokes Green's function and $\mathbf{f}$ and $\tilde{\mathbf{f}}$ are the fluid tractions at the interface from the outside and the inside of the drop. We used the velocity continuity at the interface as well as the viscosity matched condition $\lambda = 1$, the latter to eliminate the double layer integral (for details, see [74] or [68]). Following the steps detailed in [68], we expand $G_{ij}(\mathbf{x}, \mathbf{y})$ in Taylor series around the center of the drop $\mathbf{y}_c$: $G_{ij}(\mathbf{x}, \mathbf{y}) = G_{ij}(\mathbf{x}, \mathbf{y}_c) + \partial G_{ij}(\mathbf{x}, \mathbf{y}_c)/\partial y_{ck}(y_k - y_{ck}) + O(a/L)^3$, to obtain

$$u_j(\mathbf{x}) = u_j^{\infty}(\mathbf{x}) - \frac{1}{8\pi\mu} G_{ij}(\mathbf{x}, \mathbf{y}_c)\int_{A_d} \Delta f_i(\mathbf{y}) dA(\mathbf{y}) - \frac{1}{8\pi\mu}\frac{\partial G_{ij}(\mathbf{x}, \mathbf{y}_c)}{\partial y_{ck}}\int_{A_d} [\Delta f_i(\mathbf{y})(y_k - y_{ck})] dA(\mathbf{y}). \tag{A2}$$

For a force-free drop, the first term (Stokeslet) disappears. Neglecting the higher-order terms, we obtain

$$u_j(\mathbf{x}) = u_j^{\infty}(\mathbf{x}) - \frac{1}{8\pi\mu}\frac{\partial G_{ij}(\mathbf{x}, \mathbf{y}_c)}{\partial y_{ck}}\Gamma\int_{A_d} [(\nabla \cdot \mathbf{n}) n_i (y_k - y_{ck})] dA(\mathbf{y}). \tag{A3}$$

We emphasize that the above result is not exact and is valid only in the far-field $r/a \geq 1$, with r being the radial distance from the drop center, but captures the most dominant term. Noting the symmetry of the term inside the square bracket in i and k, the disturbance field, therefore, is

$$u^d \sim (\Gamma/\mu)(\nabla G)_s \text{ or } u^d/\dot{\gamma}a \sim (1/Ca)(\nabla G)_s. \tag{A4}$$

Here, $(\nabla G)_s$ is the Stokes stresslet term [74,75]. Note that the expression (A4) is not valid in the limit of $Ca \to 0$ (infinitely large interfacial tension). For a spherical drop, the coefficient of the stresslet [integral in Eq. (A3)] is isotropic and hence would not contribute to the velocity field as the stresslet is trace-free [75]. The flow remains bounded and decays faster. This fact indicates the limited validity of such order of estimate results.

For an order of estimate, we will treat the tension due to the first normal stress difference along the curved streamlines which gives rise to the enhanced zone of curved streamlines with an analogy to the interfacial tension as follows. The interfacial tension Γ acts at the interface between the drop and the surrounding media. On the other hand, the elastic tension along the curved streamlines due to the first normal stress difference is distributed in a zone of the spiraling streamline around the drop $a < r < R_{\text{spiral}}$. Although the flow around a three-dimensional deformed drop is not viscometric, we crudely approximate it as one. Furthermore, we assume a constant shear rate $\dot{\gamma}$ appropriate for the imposed rectilinear shear although the streamlines are curved by the presence of the drop, thereby allowing an expression for the first normal stress difference $N_1 = 2\lambda\mu_p\dot{\gamma}^2$ in the region around the drop $a < r < R_{\text{spiral}}$. This results in an "effective viscoelastic tension" in this region

$$\begin{aligned}\Gamma_{\text{viscoelastic}} \sim N_1\Delta r &= 2\lambda\mu_p\dot{\gamma}^2(R_{\text{spiral}} - a) \\ &= 2\mu\dot{\gamma}a(\beta Wi)\left(\frac{R_{\text{spiral}}}{a} - 1\right), \\ \Gamma^{\text{eff}} = \Gamma + \Gamma_{\text{viscoelastic}} &= \Gamma + 2\mu\dot{\gamma}a(\beta Wi)\left(\frac{R_{\text{spiral}}}{a} - 1\right) \\ &= \mu\dot{\gamma}a\left[\frac{1}{Ca} + 2(\beta Wi)\left(\frac{R_{\text{spiral}}}{a} - 1\right)\right].\end{aligned} \tag{A5}$$

Therefore, similar to Eq. (A4), with the viscoelastic tension included the disturbance velocity is

$$u^d/\dot{\gamma}a \sim (\Gamma^{\text{eff}}/\mu\dot{\gamma}a)(\nabla\bar{G})_s, \tag{A6}$$

where nondimensional Stokeslet $\bar{G} \sim a/r$ according to Eq. (A1), and $(\nabla\bar{G})_s \sim (a/r)^2$. Therefore, the disturbance velocity $u^d/\dot{\gamma}a \sim (\Gamma^{\text{eff}}/\mu\dot{\gamma}a)(a/r)^2$ deforms the rectilinear streamlines due to the imposed shear near the drop. Far away it decays as $(a/r)^2$ leading to straight streamlines there. A balance between the disturbance velocity and the rectilinear imposed shear velocity $u^{\infty}/\dot{\gamma}a = y/a \sim r/a$, at a distance

$r = R_{\text{spiral}}$ obtains

$$(\Gamma^{\text{eff}}/\mu\dot{\gamma}a)(a/R_{\text{spira}})^3 \sim 1. \tag{A7}$$

In such an approximate force balance with orders of the estimate, the exact magnitude of the terms cannot be ascertained. Therefore, we introduce an arbitrary strength for the relative magnitude of the shear as A,

$$\left[\frac{1}{Ca} + 2(\beta Wi)\left(\frac{R_{\text{spiral}}}{a} - 1\right)\right](a/R_{\text{spiral}})^3 = A, \tag{A8}$$

using Eq. (A5). Noting that the spiral region is limited in extent, A is large. For a tumbling trajectory, the spiral region needs to be at least $R_{\text{spiral}} > 2a$ [see Fig. 5(c)] to trap a second drop during the shear-induced interaction. As noted before, relation (A4) is not valid for $Ca \to 0$, with the stresslet term being identically zero in the limit. Therefore, although Eq. (A8) obtains an arbitrarily large R_{spiral}/a as $Ca \to 0$ in a Newtonian medium ($Wi = 0$), we know that R_{spiral}/a is limited to a value far less than 2 in that limit (a spherical drop). Below a critical Wi, for howsoever small Ca one does not get tumbling trajectories. In any event, using $R_{\text{spiral}}/a = 2$, we obtain from Eq. (A8),

$$Ca = \frac{1}{8A[1 - (\beta Wi)/(2A)]} = \frac{1}{8A}\left[1 + \frac{\beta Wi}{2A} + \left(\frac{\beta Wi}{2A}\right)^2 + \cdots\right], \tag{A9}$$

where noting that A is a large number, we introduced a Binomial expansion to obtain a quadratic in Wi expression for Ca, approximately seen in Fig. 7. Note that just as the problem noted above for Eq. (A8) due to the crude approximation, Eq. (A9) obtains a non-zero Ca value for $Wi = 0$ in contrast to the flow around a spherical drop or the observation in Fig. 7. For instance, in Eqs. (A4) and (A5), one assumes that the strengths of the stresslet term [e.g., the integral in Eq. (A3)] are constant, which vary with both Ca and Wi. Therefore, one cannot directly compare the prediction Eq. (A9) with the computational observation of Fig. 7. But the expression encapsulates the dynamics of the interfacial and the viscoelastic tensions, which we note from Eq. (A5) are in the ratio $\beta WiCa$ determining the streamline geometry around a drop in a viscoelastic medium.

REFERENCES

[1] Barbati, A. C., J. Desroches, A. Robisson, and G. H. McKinley, "Complex fluids and hydraulic fracturing," Ann. Rev. Chem. Biomol. Eng. **7**, 415–453 (2016).

[2] Tung, C.-K., C. Lin, B. Harvey, A. G. Fiore, F. Ardon, M. Wu, and S. S. Suarez, "Fluid viscoelasticity promotes collective swimming of sperm," Sci. Rep. **7**, 1–9 (2017).

[3] Saintillan, D., "Rheology of active fluids," Annu. Rev. Fluid Mech. **50**, 563–592 (2018).

[4] Bazaz, S. R., A. Mashhadian, A. Ehsani, S. C. Saha, T. Krüger, and M. E. Warkiani, "Computational inertial microfluidics: A review," Lab Chip **20**, 1023–1048 (2020).

[5] Zhou, J., and I. Papautsky, "Viscoelastic microfluidics: Progress and challenges," Microsyst. Nanoeng. **6**, 1–24 (2020).

[6] Zenit, R., and J. Feng, "Hydrodynamic interactions among bubbles, drops, and particles in non-Newtonian liquids," Annu. Rev. Fluid Mech. **50**, 505–534 (2018).

[7] Shaqfeh, E. S., "On the rheology of particle suspensions in viscoelastic fluids," AIChE J. **65**, e16575 (2019).

[8] Dai, S., and R. I. Tanner, "Rheology of semi-dilute suspensions with a viscoelastic matrix," Rheol. Acta **59**, 477–486 (2020).

[9] Morris, J. F., "Toward a fluid mechanics of suspensions," Phys. Rev. Fluids **5**, 110519 (2020).

[10] Li, X. Y., and K. Sarkar, "Effects of inertia on the rheology of a dilute emulsion of drops in shear," J. Rheol. **49**, 1377–1394 (2005).

[11] Li, X. Y., and K. Sarkar, "Numerical investigation of the rheology of a dilute emulsion of drops in an oscillating extensional flow," J. Non-Newtonian Fluid Mech. **128**, 71–82 (2005).

[12] D'Avino, G., and P. L. Maffettone, "Particle dynamics in viscoelastic liquids," J. Non-Newtonian Fluid Mech. **215**, 80–104 (2015).

[13] Guido, S., and M. Simeone, "Binary collision of drops in simple shear flow by computer-assisted video optical microscopy," J. Fluid Mech. **357**, 1–20 (1998).

[14] Malipeddi, A. R., and K. Sarkar, "Collective diffusivity in a sheared viscous emulsion: Effects of viscosity ratio," Phys. Rev. Fluids **4**, 093603 (2019).

[15] Malipeddi, A. R., and K. Sarkar, "Shear-induced collective diffusivity down a concentration gradient in a viscous emulsion of drops," J. Fluid Mech. **868**, 5–25 (2019).

[16] Malipeddi, A. R., and K. Sarkar, "Shear-induced gradient diffusivity of a red blood cell suspension: Effects of cell dynamics from tumbling to tank-treading," Soft Matter **17**, 8523–8535 (2021).

[17] Bretherton, F. P., "The motion of rigid particles in a shear flow at low Reynolds number," J. Fluid Mech. **14**, 284–304 (1962).

[18] Da Cunha, F., and E. Hinch, "Shear-induced dispersion in a dilute suspension of rough spheres," J. Fluid Mech. **309**, 211–223 (1996).

[19] Snijkers, F., R. Pasquino, and J. Vermant, "Hydrodynamic interactions between two equally sized spheres in viscoelastic fluids in shear flow," Langmuir **29**, 5701–5713 (2013).

[20] Batchelor, G., and J.-T. Green, "The hydrodynamic interaction of two small freely-moving spheres in a linear flow field," J. Fluid Mech. **56**, 375–400 (1972).

[21] Fahs, H., G. Ovarlez, and X. Chateau, "Pair-particle trajectories in a shear flow of a Bingham fluid," J. Non-Newtonian Fluid Mech. **261**, 171–187 (2018).

[22] Firouznia, M., B. Metzger, G. Ovarlez, and S. Hormozi, "The interaction of two spherical particles in simple-shear flows of yield stress fluids," J. Non-Newtonian Fluid Mech. **255**, 19–38 (2018).

[23] Darabaner, C., and S. Mason, "Particle motions in sheared suspensions XXII: Interactions of rigid spheres (experimental)," Rheol. Acta **6**, 273–284 (1967).

[24] Chiu, S.-H., T.-W. Pan, and R. Glowinski, "A 3D DLM/FD method for simulating the motion of spheres in a bounded shear flow of Oldroyd-B fluids," Comput. Fluids **172**, 661–673 (2018).

[25] Vázquez-Quesada, A., and M. Ellero, "SPH modeling and simulation of spherical particles interacting in a viscoelastic matrix," Phys. Fluids **29**, 121609 (2017).

[26] Yoon, S., M. Walkley, and O. Harlen, "Two particle interactions in a confined viscoelastic fluid under shear," J. Non-Newtonian Fluid Mech. **185-186**, 39–48 (2012).

[27] Choi, Y. J., M. A. Hulsen, and H. E. Meijer, "An extended finite element method for the simulation of particulate viscoelastic flows," J. Non-Newtonian Fluid Mech. **165**, 607–624 (2010).

[28] Hwang, W. R., M. A. Hulsen, and H. E. H. Meijer, "Direct simulations of particle suspensions in a viscoelastic fluid in sliding bi-periodic frames," J. Non-Newtonian Fluid Mech. **121**, 15–33 (2004).
[29] Vázquez-Quesada, A., P. Español, R. I. Tanner, and M. Ellero, "Shear thickening of a non-colloidal suspension with a viscoelastic matrix," J. Fluid Mech. **880**, 1070–1094 (2019).
[30] Dai, S., and R. I. Tanner, "Rheology of non-colloidal suspensions with viscoelastic matrices," Soft Matter **16**, 9519–9524 (2020).
[31] Sarkar, K., and W. R. Schowalter, "Deformation of a two-dimensional drop at non-zero Reynolds number in time-periodic extensional flows: Numerical simulation," J. Fluid Mech. **436**, 177–206 (2001).
[32] Aggarwal, N., and K. Sarkar, "Deformation and breakup of a viscoelastic drop in a Newtonian matrix under steady shear," J. Fluid Mech. **584**, 1–21 (2007).
[33] Taylor, G. I., "The viscosity of a fluid containing small drops of another fluid," Proc. R. Soc. London, Ser. A. **138**, 41–48 (1932).
[34] Stone, H. A., "Dynamics of drop deformation and breakup in viscous fluids," Annu. Rev. Fluid Mech. **26**, 65–102 (1994).
[35] Guido, S., "Shear-induced droplet deformation: Effects of confined geometry and viscoelasticity," Curr. Opin. Colloid Interface Sci. **16**, 61–70 (2011).
[36] Ding, Y., P. D. Howes, and A. J. deMello, "Recent advances in droplet microfluidics," Anal. Chem. **92**, 132–149 (2020).
[37] Loewenberg, M., and E. Hinch, "Collision of two deformable drops in shear flow," J. Fluid Mech. **338**, 299–315 (1997).
[38] Olapade, P. O., R. K. Singh, and K. Sarkar, "Pairwise interactions between deformable drops in free shear at finite inertia," Phys. Fluids **21**, 063302 (2009).
[39] Singh, R. K., and K. Sarkar, "Effects of viscosity ratio and three dimensional positioning on hydrodynamic interactions between two viscous drops in a shear flow at finite inertia," Phys. Fluids **21**, 103303 (2009).
[40] Sarkar, K., and R. K. Singh, "Spatial ordering due to hydrodynamic interactions between a pair of colliding drops in a confined shear," Phys. Fluids **25**, 051702 (2013).
[41] Chan, P. C.-H., and L. Leal, "An experimental study of drop migration in shear flow between concentric cylinders," Int. J. Multiphase Flow **7**, 83–99 (1981).
[42] Singh, R. K., X. Y. Li, and K. Sarkar, "Lateral migration of a capsule in plane shear near a wall," J. Fluid Mech. **739**, 421–443 (2014).
[43] Chen, Y., and C. Wang, "Hydrodynamic interaction of two deformable drops in confined shear flow," Phys. Rev. E **90**, 033010 (2014).
[44] Aggarwal, N., and K. Sarkar, "Effects of matrix viscoelasticity on viscous and viscoelastic drop deformation in a shear flow," J. Fluid Mech. **601**, 63–84 (2008).
[45] Mukherjee, S., and K. Sarkar, "Effects of matrix viscoelasticity on the lateral migration of a deformable drop in a wall-bounded shear," J. Fluid Mech. **727**, 318–345 (2013).
[46] Yuan, D., Q. Zhao, S. Yan, S.-Y. Tang, G. Alici, J. Zhang, and W. Li, "Recent progress of particle migration in viscoelastic fluids," Lab Chip **18**, 551–567 (2018).
[47] Won, D., and C. Kim, "Alignment and aggregation of spherical particles in viscoelastic fluid under shear flow," J. Non-Newtonian Fluid Mech. **117**, 141–146 (2004).
[48] Jaensson, N., M. Hulsen, and P. Anderson, "Direct numerical simulation of particle alignment in viscoelastic fluids," J. Non-Newtonian Fluid Mech. **235**, 125–142 (2016).
[49] Chilcott, M. D., and J. M. Rallison, "Creeping flow of dilute polymer solutions past cylinders and spheres," J. Non-Newtonian Fluid Mech. **29**, 381–432 (1988).
[50] Matos, H., M. Alves, and P. Oliveira, "New formulation for stress calculation: Application to viscoelastic flow in a T-junction," Numer. Heat Transfer, Part B **56**, 351–371 (2010).
[51] Mukherjee, S., and K. Sarkar, "Lateral migration of a viscoelastic drop in a Newtonian fluid in a shear flow near a wall," Phys. Fluids **26**, 103102 (2014).
[52] Aggarwal, N., and K. Sarkar, "Rheology of an emulsion of viscoelastic drops in steady shear," J. Non-Newtonian Fluid Mech. **150**, 19–31 (2008).
[53] Szabo, P., J. M. Rallison, and E. J. Hinch, "Start-up of flow of a FENE-fluid through a 4:1:4 constriction in a tube," J. Non-Newtonian Fluid Mech. **72**, 73–86 (1997).
[54] Ramaswamy, S., and L. G. Leal, "The deformation of a viscoelastic drop subjected to steady uniaxial extensional flow of a Newtonian fluid," J. Non-Newtonian Fluid Mech. **85**, 127–163 (1999).
[55] Kim, J. M., C. Kim, C. Chung, K. H. Ahn, and S. J. Lee, "Negative wake generation of FENE-CR fluids in uniform and Poiseuille flows past a cylinder," Rheol. Acta **44**, 600–613 (2005).
[56] Dou, H.-S., and N. Phan-Thien, "Negative wake in the uniform flow past a cylinder," Rheol. Acta **42**, 383–409 (2003).
[57] Oliveira, P. J., "Asymmetric flows of viscoelastic fluids in symmetric planar expansion geometries," J. Non-Newtonian Fluid Mech. **114**, 33–63 (2003).
[58] Sarkar, K., and W. R. Schowalter, "Deformation of a two-dimensional viscoelastic drop at non-zero Reynolds number in time-periodic extensional flows," J. Non-Newtonian Fluid Mech. **95**, 315–342 (2000).
[59] Tryggvason, G., B. Bunner, A. Esmaeeli, D. Juric, N. Al-Rawahi, W. Tauber, J. Han, S. Nas, and Y.-J. Jan, "A front-tracking method for the computations of multiphase flow," J. Comput. Phys. **169**, 708–759 (2001).
[60] Unverdi, S. O., and G. Tryggvason, "A front-tracking method for viscous, incompressible, multi-fluid flows," J. Comput. Phys. **100**, 25–37 (1992).
[61] Li, X., and K. Sarkar, "Drop dynamics in an oscillating extensional flow at finite Reynolds numbers," Phys. Fluids **17**, 027103 (2005).
[62] Towns, J., T. Cockerill, M. Dahan, I. Foster, K. Gaither, A. Grimshaw, V. Hazlewood, S. Lathrop, D. Lifka, G. D. Peterson, R. Roskies, J. R. Scott, and N. Wilkins-Diehr, "XSEDE: Accelerating scientific discovery," Comput. Sci. Eng. **16**, 62–74 (2014).
[63] Singh, R. K., and K. Sarkar, "Hydrodynamic interactions between pairs of capsules and drops in a simple shear: Effects of viscosity ratio and heterogeneous collision," Phys. Rev. E **92**, 063029 (2015).
[64] Subramanian, G., and D. L. Koch, "Heat transfer from a neutrally buoyant sphere in a second-order fluid," J. Non-Newtonian Fluid Mech. **144**, 49–57 (2007).
[65] D'Avino, G., M. A. Hulsen, F. Snijkers, J. Vermant, F. Greco, and P. L. Maffettone, "Rotation of a sphere in a viscoelastic liquid subjected to shear flow. Part I: Simulation results," J. Rheol. **52**, 1331–1346 (2008).
[66] Subramanian, G., and D. L. Koch, "Centrifugal forces alter streamline topology and greatly enhance the rate of heat and mass transfer from neutrally buoyant particles to a shear flow," Phys. Rev. Lett. **96**, 134503 (2006).
[67] Subramanian, G., and D. L. Koch, "Inertial effects on the transfer of heat or mass from neutrally buoyant spheres in a steady linear velocity field," Phys. Fluids **18**, 073302 (2006).
[68] Singh, R. K., and K. Sarkar, "Inertial effects on the dynamics, streamline topology and interfacial stresses due to a drop in shear," J. Fluid Mech. **683**, 149–171 (2011).
[69] Yang, M., and E. S. G. Shaqfeh, "Mechanism of shear thickening in suspensions of rigid spheres in Boger fluids. Part I: Dilute suspensions," J. Rheol. **62**, 1363–1377 (2018).
[70] Leal, L. G., "Flow induced coalescence of drops in a viscous fluid," Phys. Fluids **16**, 1833–1851 (2004).

[71] Baldessari, F., and L. G. Leal, "Effect of overall drop deformation on flow-induced coalescence at low capillary numbers," Phys. Fluids **18**, 013602 (2006).

[72] Abdelwahed, W., G. Degobert, S. Stainmesse, and H. Fessi, "Freeze-drying of nanoparticles: Formulation, process and storage considerations," Adv. Drug Delivery Rev. **58**, 1688–1713 (2006).

[73] Taylor, G. I., "The formation of emulsions in definable fields of flow," Proc. R. Soc. London A **146**, 501–523 (1934).

[74] Pozrikidis, C., *Boundary Integral and Singularity Methods for Linearized Viscous Flow* (Cambridge University, Cambridge, 1992), Vol. 259, p. xi.

[75] Kim, S., and S. Karrila, *Microhydrodynamics: Principles and Selected Applications* (Dover, New York, 2005).